

A Structural Investigation of $\text{Ga}_{3-x}\text{In}_{5+x}\text{Sn}_2\text{O}_{16}$

D. D. Edwards,¹ T. O. Mason,² W. Sinkler, and L. D. Marks

Department of Materials Science and Engineering, Northwestern University, Evanston, Illinois 60208

and

F. Goutenoire³ and K. R. Poeppelmeier

Department of Chemistry, Northwestern University, Evanston, Illinois 60208

Received January 20, 1998; accepted April 23, 1998

The structure of the recently reported transparent conductor, $\text{Ga}_{3-x}\text{In}_{5+x}\text{Sn}_2\text{O}_{16}$ ($0.3 < x < 1.6$), was established by a combination of high-resolution electron microscopy, convergent-beam electron diffraction, and Rietveld analysis of powder diffraction data (X-ray and time-of-flight neutron methods). This “T-phase” compound has an anion-deficient fluorite-derivative structure whose space group is $I4_1/a$. Although there are similarities to the parent oxide structures, the T-phase lacks one of the distorted InO_6 octahedra observed in In_2O_3 , which may account for its inability to be donor-doped by Sn. © 1998 Academic Press

INTRODUCTION

Recently, we identified a new transparent conductor in the $\text{Ga}_2\text{O}_3\text{--In}_2\text{O}_3\text{--SnO}_2$ system (1). This new phase, referred to as the T-phase because of its tetragonal structure, can also be expressed as $\text{Ga}_{3-x}\text{In}_{5+x}\text{Sn}_2\text{O}_{16}$ ($0.3 < x < 1.6$). The T-phase has excellent transparency throughout most of the visible region with a room-temperature conductivity as high as 375 S/cm after annealing in a reducing atmosphere. However, the conductivity is an order of magnitude lower than that of Sn-doped In_2O_3 , the most widely used commercial transparent conducting oxide.

A better understanding of the T-phase crystal structure is an important step in identifying strategies to improve its conductivity. This paper reports on the structure determination of $\text{Ga}_{3-x}\text{In}_{5+x}\text{Sn}_2\text{O}_{16}$ ($x = 1.0$), or $\text{Ga}_2\text{In}_6\text{Sn}_2\text{O}_{16}$, using high-resolution transmission electron microscopy (HREM), convergent-beam electron diffraction (CBED),

and Rietveld analysis of powder diffraction data (X-ray and time-of-flight neutron methods).

EXPERIMENTAL

T-phase samples were prepared by solid state reaction from commercially obtained oxide powders ($> 99.99\%$ purity on a cation basis, Aldrich Chemical Co.). The powders were dried at 700°C overnight and stored in a desiccator prior to use. Appropriate amounts of each of the oxides were weighed, moistened with acetone, and ground together with an agate mortar and pestle. The mixed powder was dried and pressed into 1-inch-diameter pellets. The pellets were buried in a powder bed of the same composition inside high-density alumina crucibles. The pellets were reacted at 1250°C for up to 2 weeks with intermediate grindings. After the final firing, the samples were ground to provide powder suitable for the subsequent analyses. The resulting samples were light green, as is typical of transparent conductors.

X-ray diffraction analysis of the resulting powders was conducted using a Scintag XDS 2000 diffractometer (Scintag Inc., USA) using $\text{CuK}\alpha$ radiation (40 kV, 20 mA). For routine phase analysis and lattice-parameter measurements, powder was mounted on a glass slide with double-sided adhesive tape. Lithium fluoride was used as an internal standard. Data was collected over $10\text{--}70^\circ 2\theta$ in 0.05° steps, counting for 1 s per step. Commercial software was used to calculate the position of the reflections with respect to the LiF standard. Lattice parameters were determined using least-squares analysis. For Rietveld analysis, the powder was mounted in a flat, plastic sample holder with a recessed cavity (ca. 1 in. \times 1 in. \times 1/8 in.). Because the diffractometer requires vertical placement of the sample, Kapton film (Spex Industries, USA) was used to hold the powder sample in place. Data was collected over $5\text{--}140^\circ 2\theta$ in 0.02° steps, counting for 7–8 s per step.

¹New York State College of Ceramics at Alfred University, Department of Ceramic Engineering and Materials Science, Alfred, NY 14802.

²Author to whom correspondence should be addressed.

³Laboratoire des Fluorures, URA-CNRS 449, Faculté des Sciences—Université du Maine, 72017 Le Mans Cedex, France.

HREM was performed using an Hitachi H9000 high-resolution microscope operated at 300 kV. Transmission electron diffraction and CBED were obtained with an Hitachi HF2000 field emission analytical TEM, using a Gatan liquid nitrogen cooled specimen holder. For specimen preparation, a small amount of powder was ground with a mortar and pestle under dry methanol to produce a suspension. A drop of the suspension was deposited on a 1000 mesh copper grid and dried.

Time-of-flight neutron diffraction data was collected at Argonne National Laboratory's Intense Pulsed Neutron Source (2). Rietveld analysis of X-ray diffraction and TOF neutron data were carried out separately using the GSAS (General Structural Analysis System) suite of programs (3) For X-ray diffraction data, refined global parameters included lattice parameters, up to five background coefficients, up to twelve profile coefficients (psuedo-Voight function), and a scaling factor. For neutron diffraction data, refined global parameters included the lattice parameters, up to twelve background coefficients, and two absorption coefficients. Of the twelve coefficients associated with the neutron peak-profile function, only one coefficient, related to peak width, was refined. The X-ray scattering factors for Ga^{3+} , In^{3+} , and Sn^{4+} and the neutron scattering lengths for Ga, In, Sn, and O were taken from the "International Tables of Crystallography" (4). The X-ray scattering factor for O^{2-} was taken from Hovestreydt (5).

RESULTS AND DISCUSSION

Structure Determination

The solid-solubility range of the T-phase, or $\text{Ga}_{3-x}\text{In}_{5+x}\text{Sn}_2\text{O}_{16}$, extends from $x = 0.3$ to $x = 1.6$ at 1250°C (6). Over this solubility range, the lattice parameters can be expressed approximately as $a = 11.110 + 0.0688x$ and $c = 9.949 + 0.0875x$, with both a and c given in Å. Figure 1 compares the X-ray diffraction pattern of $\text{Ga}_2\text{In}_6\text{Sn}_2\text{O}_{16}$, or $x = 1.0$, to the X-ray diffraction pattern of In_2O_3 . The location of the four most intense peaks is similar in both patterns, but the low-intensity peaks indicate that $\text{Ga}_{3-x}\text{In}_{5+x}\text{Sn}_2\text{O}_{16}$ is tetragonal whereas In_2O_3 is cubic. The diffraction pattern of $\text{Ga}_2\text{In}_6\text{Sn}_2\text{O}_{16}$ is indexed in Table 1. Additional confirmation of the tetragonal unit cell was obtained using selected area electron diffraction patterns.

A preliminary structural model was identified by comparing the X-ray diffraction patterns of T-phase samples to those of In_2O_3 . The similarity between the diffraction patterns (Fig. 1) indicates that the cation arrangement of the T-phase is closely related to that of In_2O_3 which, in turn, is related to the cubic fluorite structure. Comparison of the T-phase lattice parameters to that of In_2O_3 suggests that the two structures are related by a rotation about the c -axis as shown in Fig 2. The lattice vectors of the new cell are

TABLE 1
Indexing of $\text{Ga}_2\text{In}_6\text{Sn}_2\text{O}_{16}$ (Experimental Values)

h	k	l	d (Å)	I/I_0
2	1	1	4.4734	2
2	0	2	3.7349	2
3	0	1	3.4907	2
3	1	2	2.8904	100
2	1	3	2.7795	2
4	1	1	2.6175	2
4	2	0	2.5011	26
1	1	4	—	—
3	2	3	2.2751	2
4	2	2	2.2385	3
4	1	3	2.106	3
5	2	1	2.0309	3
5	0	3	1.8592	3
4	2	4	1.7700	36
5	4	1	1.7202	3
5	1	4	—	—
4	1	5	1.6123	3
7	0	1	—	—
2	2	6	1.5477	2
7	2	1	—	—
5	5	2	1.5072	21
6	2	4	1.4437	6

expressed in terms of the old cell as:

$$\begin{pmatrix} a_t \\ b_t \\ c_t \end{pmatrix} = \begin{pmatrix} 1 & \frac{1}{2} & 0 \\ -\frac{1}{2} & 1 & 0 \\ 0 & 0 & 1 \end{pmatrix} \begin{pmatrix} a_c \\ b_c \\ c_c \end{pmatrix}. \quad [1]$$

Figure 3 shows an HREM image taken along the tetragonal c axis. The image was taken from a thin region near

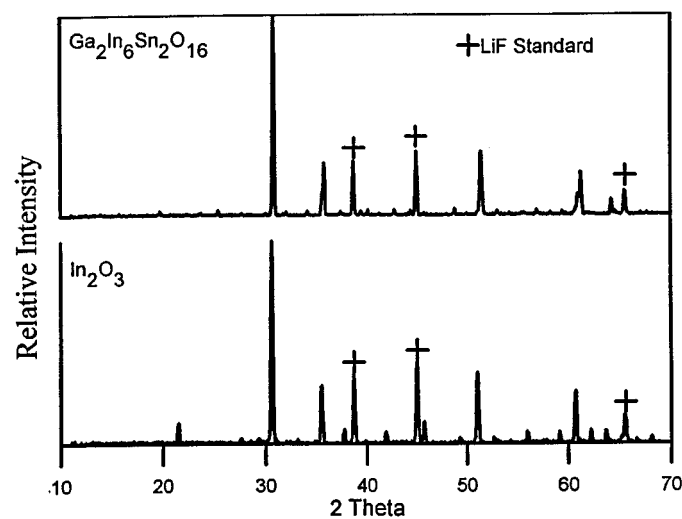


FIG. 1. X-ray powder diffraction pattern of $\text{Ga}_2\text{In}_6\text{Sn}_2\text{O}_{16}$ and In_2O_3 .

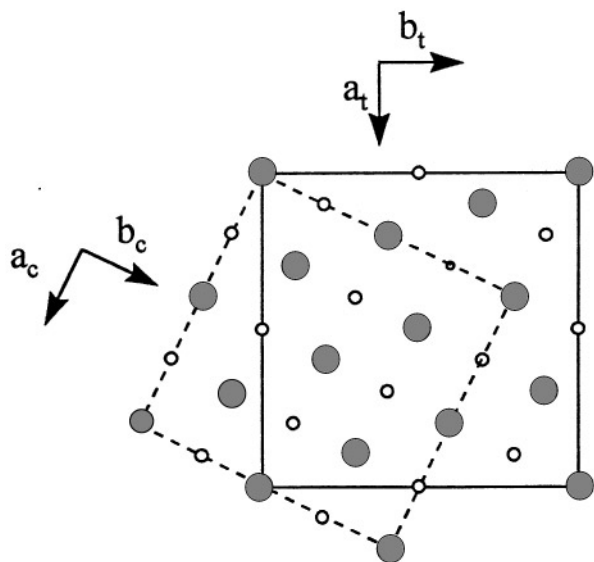


FIG. 2. Idealized cation positions of the tetragonal $\text{Ga}_2\text{In}_6\text{Sn}_2\text{O}_{16}$ structure in reference to the parent cubic fluorite structure. Cation positions, presented as grey and open circles, are located at $z = 0, \frac{1}{2}$ and $z = \frac{1}{4}, \frac{3}{4}$ respectively. The solid line indicates projected tetragonal unit cell. The dashed line indicates projected cubic (fluorite) unit cell.

Scherzer defocus. Under these conditions, areas of large electrostatic potential, i.e., the heavier cation positions in the projected structure, are expected to appear dark in the image. The intensity minima in Fig. 3 are consistent with projected cation positions of a fluorite-like structure after rotation using Eq. [1], thus providing a preliminary confirmation of the model.

Several space groups were eliminated from consideration based on the X-ray diffraction data and the model shown in Fig. 2. The exclusive presence of hkl with $h + k + l = 2n$ (Table 1) indicates a body-centered cell (I). The presence of

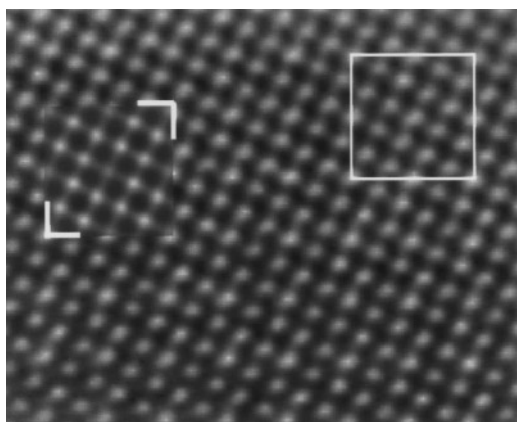


FIG. 3. HREM micrograph of the T-phase along $[001]$. Square at upper right indicates unit cell ($a = 11.110 \text{ \AA}$). Inset is a multislice simulation of the neutron-refined structure for 32 \AA thickness and 500 \AA defocus.

an hkl reflection with $2h + l \neq 4n$ indicates that the structure does not contain a diamond glide plane. The cation arrangement shown in Fig. 2 does not possess mirror planes parallel to (100) , (010) , and (110) or a twofold rotational axis about $[110]$, leaving $I4$, $I4$, $I4/m$, $I4_1$, and $I4_1/a$ as possible space groups, or 4 , $\bar{4}$, and $4/m$ as possible point groups.

Convergent-beam electron diffraction (CBED) analysis was used to identify the appropriate space group. Figure 4a shows a $[\bar{1}10]$ select area diffraction pattern (SADP), and Fig. 4b shows the corresponding Kossel-Möllenstedt CBED pattern. The symmetry of the pattern in Fig. 4b shows a single horizontal mirror plane perpendicular to the c axis. While there also appears to be a vertical mirror plane, this was not present in the higher-order Laue zone reflections (not shown). Moreover, the presence of a second mirror plane conflicts with the three possible point groups (4 , $\bar{4}$, $4/m$). The presence of mirror whole-pattern symmetry in the $[110]$ is sufficient, given the limitations of the three possible point groups, to identify the diffraction group as 2_Rmm_R (7, 8). This further eliminates the point groups 4 and $\bar{4}$, and identifies the point group as $4/m$.

Whereas the SADP in Fig. 4a has the appearance of a primitive lattice with no missing spots, some of the spots in the pattern are kinematically forbidden reflections which are present due to dynamical effects. For example, the dark lines bisecting the (330) and $(\bar{3}\bar{3}0)$ diffraction spots in Fig. 4b (arrows) are consistent with Gjønnes-Moodie lines (9) and indicate that these are dynamically allowed, kinematically forbidden reflections. Orientation of a mirror plane parallel to the Gjønnes-Moodie lines in a CBED pattern of group 2_Rmm_R indicates that the space group contains a glide plane parallel to the beam and perpendicular to the c axis in the present case (8). The only body-centered space group in the $4/m$ point group which has such a glide plane is $I4_1/a$.

Given the fluorite parent structure and the space group $I4_1/a$, a primary consideration in solving the new structure was determining the anion arrangement. The tetragonal cell derived from the fluorite parent structure has 40 cation sites (Fig. 2) and 80 anion sites that can be placed in the $I4_1/a$ space group as summarized in Table 2. (Note that the atomic positions in Table 2 are shifted by $[0, -\frac{1}{4}, \frac{1}{8}]$ with respect to the model shown in Fig. 2 based on the convention used by the Rietveld-refinement software.)

According to the stoichiometry of the $\text{Ga}_2\text{In}_6\text{Sn}_2\text{O}_{16}$, only 64 anions are associated with 40 cations ($Z = 4$), suggesting that $\frac{1}{5}$ of the anion sites is vacant, i.e., one set of 16 anion sites is vacant. With cations and anions in the ideal fluorite positions, placement of the anion vacancies on each of the anion sites (Table 2) results in three distinct configurations, as summarized in Table 3.

Configuration A, resulting from vacancies at O(1), was considered a possibility because of its simplicity, possessing only two types of cation coordination polyhedra. However, the resulting MO_6 polyhedra are unlike those observed in

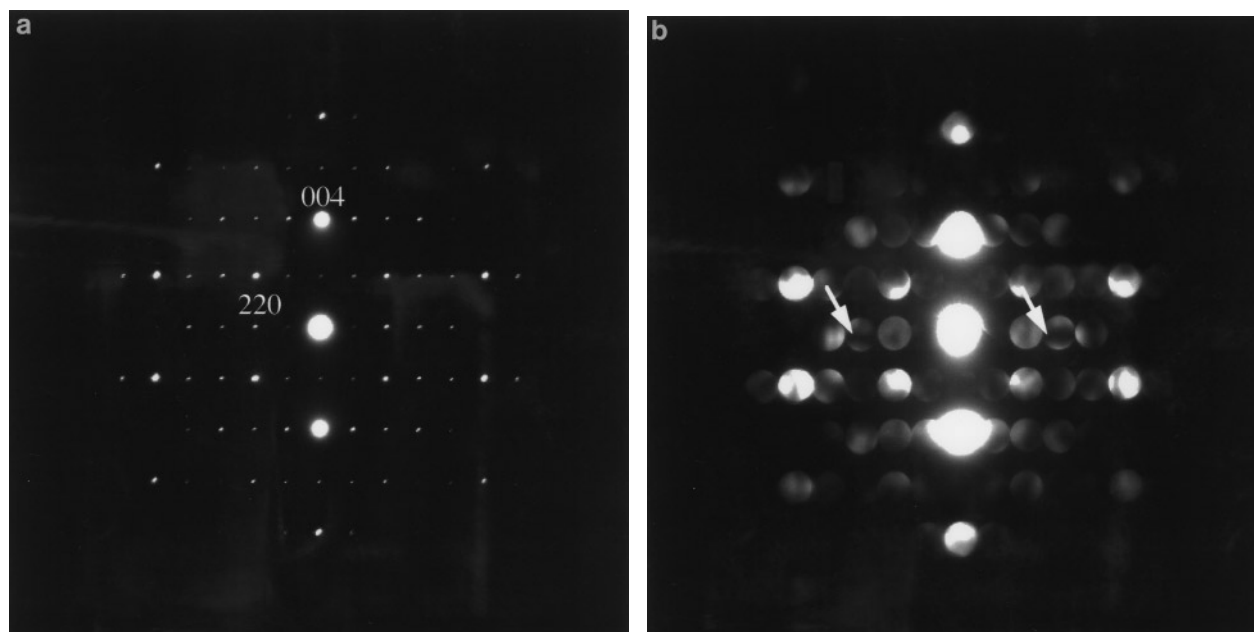


FIG. 4. (a) Selected area diffraction pattern of a T-phase $[\bar{1}10]$ zone axis pattern. (b) Kossel-Möllenstedt CBED pattern showing horizontal mirror plane symmetry. The arrows point to Gjønnes-Mödie lines bisecting the (330) and $(\bar{3}\bar{3}0)$ diffraction discs, which indicate that these are dynamically allowed, kinematically forbidden reflections.

previously reported anion-deficient-fluorite structures, such as In_2O_3 , $\text{In}_4\text{Sn}_3\text{O}_{12}$, $\text{Y}_2\text{Sn}_2\text{O}_7$, or $\text{WIn}_6\text{O}_{12}$. Most reported anion-deficient-fluorite structures have anion vacancies located at the body-diagonal (Fig. 5a) or at the face-diagonal (Fig. 5b) of the fluorite parent cube whereas vacancy placement on O(1) results in anion vacancies located along the edge of the parent fluorite cube (Fig. 5c).

Configurations B and C are considerably more complex, possessing cations with 4-fold, 6-fold, 7-fold, and 8-fold coordination. The primary difference between the models lies in the resulting MO_6 polyhedra. Configuration B, with vacancies at O(2) or at O(3), possesses MO_6 polyhedra like that illustrated in Fig. 5c whereas configuration C, with

vacancies at O(5) or O(4), possesses MO_6 polyhedra like that illustrated in Fig. 5a.

Another consideration in solving the T-phase structure was determining whether or not the cations were ordered. Since gallium is the smallest cation, it was expected to adopt lower coordination than the indium or tin. Likewise, indium was expected to adopt a higher coordination than gallium or tin.

Preliminary Rietveld analysis of X-ray data provided convincing evidence for anion-vacancy placement at O(5) (configuration C). A refinement was initiated with 8 Ga^{3+} and 32 Sn^{4+} (or In^{3+}) statistically distributed on the four cation sites and 64 O^{2-} statistically distributed over the five anion sites. (The X-ray scattering factors of Sn^{4+} and In^{3+}

TABLE 2
Ideal Fluorite Structure Atom Positions in $I4_1/a$ Space Group

Atoms	Site	x	y	z
$M(1)$	$4a$	0.00	0.25	0.625
$M(2)$	$4b$	0.00	0.25	0.125
$M(3)$	$16f$	0.30	0.35	0.125
$M(4)$	$16f$	0.20	0.65	0.125
O(1)	$16f$	0.25	0.00	0.000
O(2)	$16f$	0.05	0.10	0.000
O(3)	$16f$	0.55	0.10	0.000
O(4)	$16f$	0.85	0.20	0.000
O(5)	$16f$	0.35	0.20	0.000

TABLE 3
Cation Coordination Resulting from Placement of Anion Vacancies

Configuration	Vacancy placement	$M(1)$	$M(2)$	$M(3)$	$M(4)$
A	O(1)	8	8	6^a	6^a
B	O(2) or O(3)	4	8	7	6^a
C	O(4) or O(5)	4	8	7	6^b

^aAnion vacancies at the side of the parent coordination cube.

^bAnion vacancies at the body diagonal of the parent coordination cube.

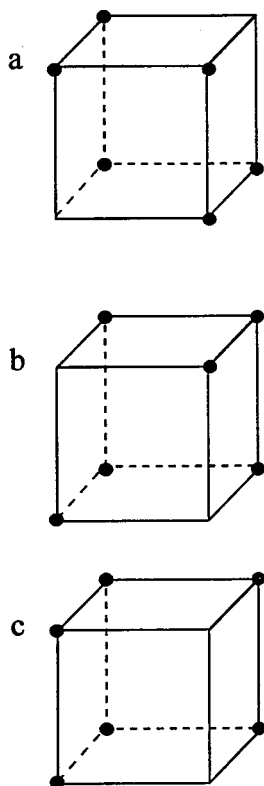


FIG. 5. Sixfold coordination polyhedra resulting from anion-vacancy placement along (a) the body-diagonal of parent cube, (b) the face-diagonal of parent coordination cube, and (c) the edge of parent cube.

are sufficiently similar that they can not be distinguished from one another.) Refinement of the cation positions and occupancies indicated a strong tendency for Ga^{3+} to reside on $M(1)$ and for Sn^{4+} (or In^{3+}) to reside on $M(2)$. Using the refined cation positions, a Fourier difference map was constructed for a partial structure with Ga^{3+} on $M(1)$, with Sn^{4+} or In^{3+} on $M(2)$, the remaining cations statistically distributed on $M(3)$ and $M(4)$, and all of the anions sites vacant. The map indicated high electron density on all anion sites except O(5).

Subsequent analysis of the X-ray diffraction data was conducted in $I4_1/a$ with full occupancy of O(1), O(2), O(3), and O(4) and complete vacancy of O(5). Refined atom parameters included general atomic positions, occupancy of $M(3)$ and $M(4)$, and isotropic thermal parameters. The occupancies of $M(1)$ and $M(2)$ were not refined. Ga^{3+} , the smallest cation, was placed on the site with 4-fold coordination and In^{3+} , the largest cation, was placed on the site with 8-fold coordination. The remaining cations were statistically distributed over the two general cation sites with 6-fold and 7-fold coordination.

Although refinement led to a reasonable fit to the X-ray data, as shown in Fig. 6, there were several concerns regarding the refined solution. First, the solution gave little in-

formation about the cation distribution. The distribution of In^{3+} and Sn^{4+} could not be determined since the X-ray scattering factors are similar to one another. Although attempts were made to identify the distribution of Ga^{3+} on $M(3)$ and $M(4)$ by refining the ratio of Ga^{3+} to the combined sum of Sn^{4+} and In^{3+} , the thermal parameters of $M(3)$ and $M(4)$ were highly correlated to occupancy. Constraining the thermal parameters of $M(3)$ and $M(4)$ to be equal led to a near-statistical distribution of cations, which is unlikely considering the size differences. Second, the refined atomic positions were questionable, primarily owing to the low X-ray scattering factor of O^{2-} . Refinements incorporating independent oxygen thermal parameters often diverged, although the fit to the data did not change significantly. Constraining the thermal parameters of the oxygen atoms to be equal allowed refinements to proceed smoothly, but some of the resulting M -O bond lengths were shorter than expected.

Many of the concerns associated with the refinement of the X-ray data were overcome by using neutron data. Refinements were initiated in $I4_1/a$ using the atomic positions obtained from the X-ray refinements and the following atom distribution: Ga on $M(1)$, In on $M(2)$, the remaining cations on $M(3)$ and $M(4)$, and oxygen on O(1)–O(4). After refinement of the atomic positions, a series of trial refinements were conducted to test various features of the structure. In the first trial refinement, oxygen was placed on all of the possible oxygen sites O(1)–O(5), and refinement confirmed the vacancy of O(5). In the second trial refinement, the occupancies of $M(3)$ and $M(4)$ were refined along with other atom parameters using overall chemical composition as a constraint. A negative occupancy of $M(3)$ by Ga suggested that Ga resides preferentially on the site with 6-fold coordination as expected from size considerations. In a third trial refinement, the In and Sn were statistically distributed on $M(2)$, $M(3)$, and $M(4)$. Using overall chemical composition as a constraint, the refinement indicated a strong preference for In to reside on $M(2)$ as expected from size considerations.

The final refinement of the neutron data was initiated with the atoms distributed as follows: Ga on $M(1)$ and $M(4)$, In on $M(2)$, the remaining Sn and In statistically distributed on $M(3)$ and $M(4)$, and oxygen on O(1)–O(4). Atom parameters refined included atomic position, isotropic thermal parameters, and the distribution of In and Sn on $M(3)$ and $M(4)$. Overall chemical composition was used as a constraint. The thermal parameters of $M(1)$ and $M(4)$ refined to negative values and were subsequently fixed at a value of 0.004 \AA^2 , the value reported for tetrahedral and octahedral sites in $\beta\text{-Ga}_2\text{O}_3$ (10).

As shown in Fig. 7, the resulting refinement led to an excellent fit to the experimental data with R values of $R_{\text{wp}} = 4.37\%$ and $R_{\text{p}} = 3.05\%$. As with the X-ray data, there was some evidence of impurity phases. The largest

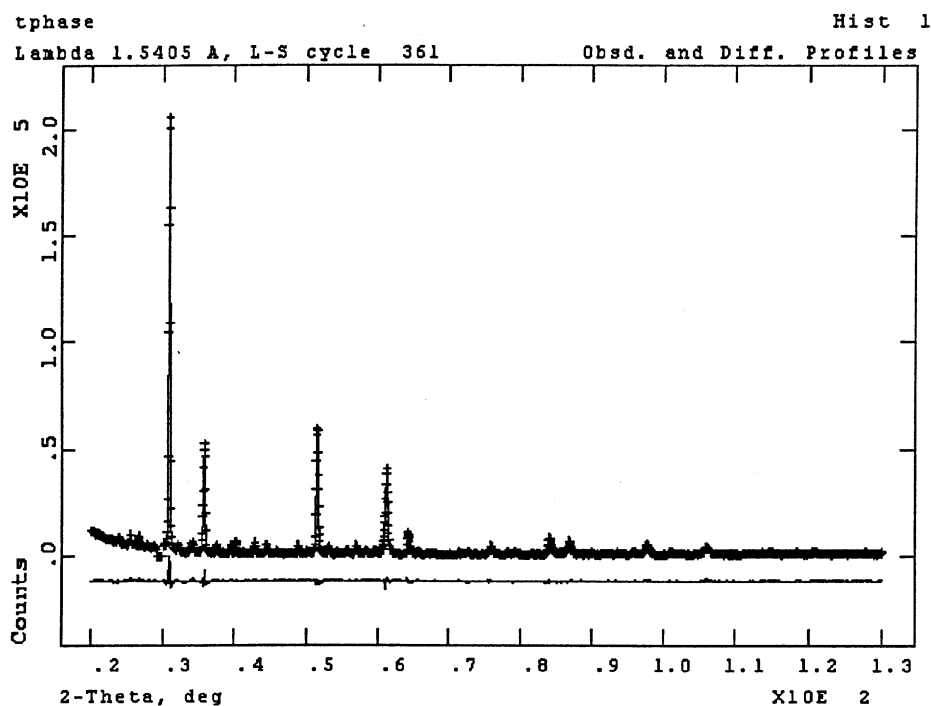


FIG. 6. Observed, calculated, and difference X-ray powder diffraction patterns for $\text{Ga}_2\text{In}_6\text{Sn}_2\text{O}_{16}$. The observed data are indicated by crosses, and the calculated pattern, by a solid line.

peak, near 16 ms or 2.15 Å, was excluded from refinement although this had little effect on the refined parameters and associated R values. As shown in Table 4, the refinement indicated a nonstatistical distribution of In and Sn on $M(3)$ and $M(4)$. As expected from size considerations, In resides preferentially on $M(3)$, the site with 7-fold coordination. (A

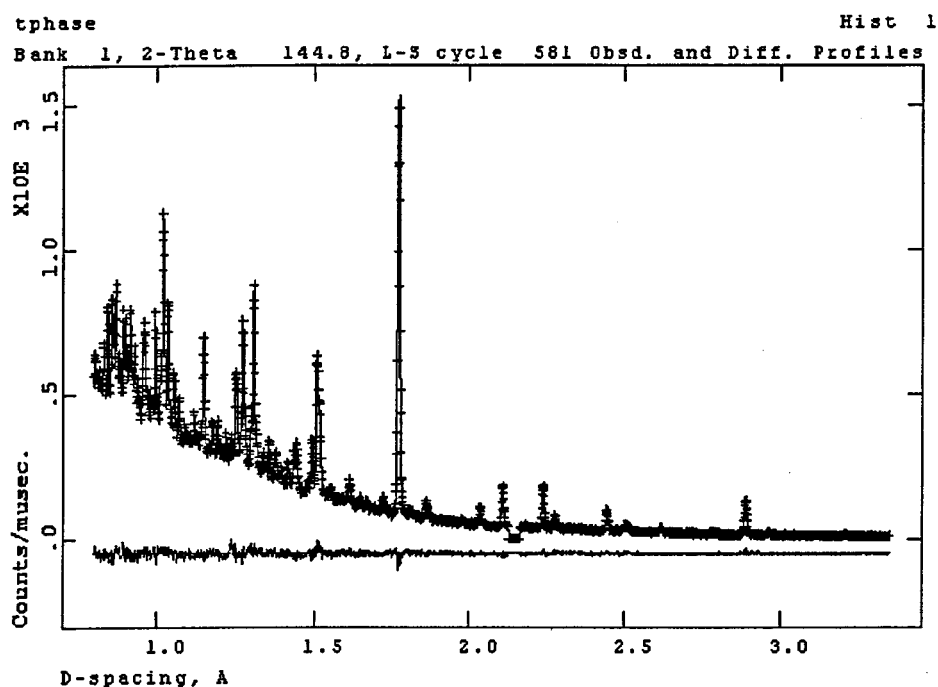


FIG. 7. Observed, calculated, and difference TOF neutron powder diffraction patterns for $\text{Ga}_2\text{In}_6\text{Sn}_2\text{O}_{16}$. The observed data are indicated by crosses, and the calculated pattern, by a solid line.

TABLE 4
Structural Parameters for $\text{Ga}_2\text{In}_6\text{Sn}_2\text{O}_{16}$
(Space Group $I4_1/a$; $a = 11.1800(1)$ Å, $c = 10.0406(2)$ Å)

Atom	Site	x	y	z	$U \times 100$ (Å ²)	Occupancy
Ga(1)	4a	0.0 ^a	0.25 ^a	0.625 ^a	0.40 ^a	1 ^a
In(2)	4b	0.0 ^a	0.25 ^a	0.125 ^a	0.39(24)	1 ^a
In(3)	16f	0.2944(6)	0.3728(4)	0.1491(4)	0.28(14)	0.92(3)
Sn(3)	16f	0.2944(6)	0.3728(4)	0.1491(4)	0.28(14)	0.08(3)
Ga(4)	16f	0.1946(4)	0.6633(3)	0.1282(4)	0.40 ^a	0.250
In(4)	16f	0.1946(4)	0.6633(3)	0.1282(4)	0.40 ^a	0.33(3)
Sn(4)	16f	0.1946(4)	0.6633(3)	0.1282(4)	0.40 ^a	0.42(3)
O(1)	16f	0.2747(4)	0.0395(4)	-0.0084(4)	0.51(9)	1 ^a
O(2)	16f	0.0406(5)	0.1161(4)	-0.0269(4)	0.59(10)	1 ^a
O(3)	16f	0.5333(4)	0.1174(4)	-0.0191(5)	0.29(9)	1 ^a
O(4)	16f	0.8070(4)	0.1946(4)	-0.0001(4)	1.11(11)	1 ^a

$R_{\text{wp}} = 4.37\%$; $R_{\text{wp}} = 3.05\%$; $\chi^2 = 1.504$

^aParameters held constant during refinement.

slightly lower distribution of In on $M(3)$, 0.85 vs 0.92, was obtained when the thermal parameters of $M(1)$ and $M(4)$ were not fixed and allowed to refine to negative values.)

The cation positions indicated by the refinement of the neutron data were in excellent agreement with those obtained from the refinement of X-ray diffraction data (not shown). While there were some discrepancies among the refined oxygen positions, this is understandable considering that oxygen has a relatively low X-ray scattering factor. To further test the validity of the atom parameters summarized in Table 4, another refinement of the X-ray data was conducted by holding the atom parameters constant and refining the global parameters. The resulting fit to experimental data was comparable to that shown in Fig. 6 with $R_{\text{wp}} = 11.47\%$ and $R_p = 7.97\%$.

As a final confirmation of the structure model, multislice calculations were performed for comparison with the HREM through-focus image series. Using the neutron-refined structure, agreement was obtained between HREM images and the multislice calculations. As an example, a calculated image for 500 Å defocus and 46 Å thickness is shown as an inset to Fig. 3 and gives a good match to the experimental image.

Structure Description

Crystallizing in $I4_1/a$ with $Z = 4$, the T-phase or $\text{Ga}_{3-x}\text{In}_{5+x}\text{Sn}_2\text{O}_{16}$ can be viewed as having an anion-deficient fluorite structure. The tetragonal structure is derived from a cubic-fluorite parent structure by a 26.6° rotation about the c -axis and removal of $\frac{1}{5}$ of the anions. The atomic positions in the tetragonal phase are shifted as much as 0.52 Å from the parent fluorite structure, but the structure retains alternating layers of cations and anions along

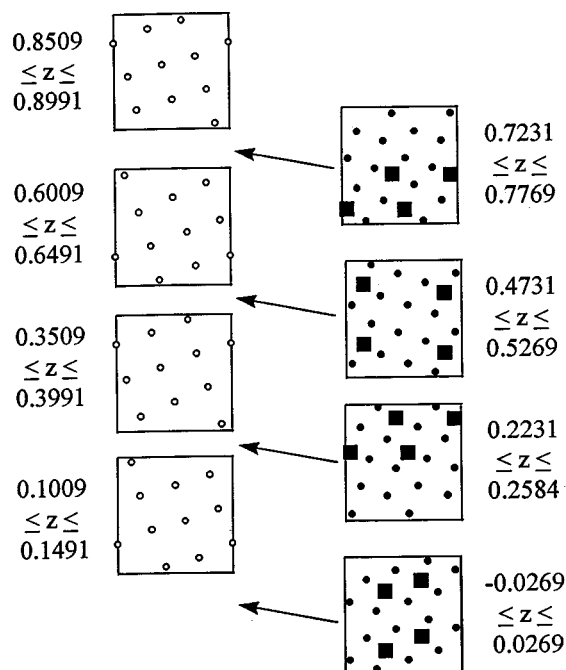


FIG. 8. Projection of cation and anion layers in $\text{Ga}_2\text{In}_6\text{Sn}_2\text{O}_{16}$ along the c axis. Open circles represent cations, filled circles represent anions, and filled squares represent "anion vacancies" in reference to the fluorite parent structure.

the c axis as illustrated in Fig. 8. In general, the anions are shifted towards the formal vacancies, and the cations are shifted away from the formal vacancies.

As a result of the anion-vacancy arrangement, cations possess 4-fold, 6-fold, 7-fold, and 8-fold coordination. $\text{Ga}_2\text{In}_6\text{Sn}_2\text{O}_{16}$ exhibited a strong tendency towards size-dependent cation ordering, with complete occupancy of the 4-fold and 8-fold sites by Ga and In, respectively. However, there was some minor cation disorder on the sites with 6-fold and 7-fold coordination. In a fully ordered system, the site with 7-fold coordination is expected to be occupied by In whereas the 6-fold site is expected to be occupied by all three cations. Based on the solid-solubility range of $\text{Ga}_{3-x}\text{In}_{5+x}\text{Sn}_2\text{O}_{16}$ ($0.3 < x < 1.6$), the weighted average of the trivalent cation radii on the site with 6-fold coordination would be 0.65–0.74 Å, a range which is centered about the radius of Sn^{4+} (0.69 Å).

Table 5 summarizes the M -O bond lengths associated with each of the coordination polyhedra. For comparison, various M -O bond lengths found in related materials are summarized in Table 6.

In $\text{Ga}_2\text{In}_6\text{Sn}_2\text{O}_{16}$, the MO_4 polyhedra are nearly regular tetrahedra with $M(1)$ -O(3) bond lengths of 1.862 Å and O(3)- $M(1)$ -O(3) bond angles ranging from 109 to 110°. The bond lengths are comparable to those measured for the tetrahedra in β - Ga_2O_3 (10). The tetrahedra share corners exclusively with MO_6 polyhedra and separate pairs of edge

TABLE 5
Select Bond Lengths

Polyhedra	Bond	Length (Å)
MO_4	Ga(1)–O(3)	1.862(4)
MO_8	In(2)–O(2)	2.185(4)
	In(2)–O(4)	2.570(4)
	Average	2.378
MO_7	M(3)–O(1)	2.223(6)
	M(3)–O(1)	2.344(7)
	M(3)–O(2)	2.394(8)
	M(3)–O(2)	2.135(7)
	M(3)–O(3)	2.561(7)
	M(3)–O(4)	2.023(6)
	M(3)–O(4)	2.110(8)
	Average	2.256
MO_6	M(4)–O(1)	2.040(6)
	M(4)–O(1)	2.037(6)
	M(4)–O(2)	2.061(7)
	M(4)–O(3)	2.073(6)
	M(4)–O(3)	2.277(7)
	M(4)–O(4)	2.046(6)
	Average	2.089

sharing MO_6 polyhedra. Connection of edge sharing MO_6 polyhedra by corner sharing MO_4 tetrahedra is also observed in β -gallia where the $M_{\text{oct}}-M_{\text{tet}}$ bond lengths (3.28–3.45 Å) are comparable to those observed in the present study (3.437 Å). In addition to sharing corners with the tetrahedra, the MO_6 polyhedra share edges with MO_8 and MO_7 polyhedra and corners with MO_7 and other MO_6 polyhedra.

In the MO_6 polyhedra, both the cations and anions are shifted from their parent fluorite structure to form distorted octahedra. The $M(4)-O$ bond lengths with an average of

TABLE 6
Reported $M-O$ Bond Lengths for Related Structures

Coordination Bond	polyhedra	Compound	$M-O$ bond lengths (Å)	Reference
Ga–O	MO_4	Ga_2O_3	Range: 1.80–1.85 Average: 1.83	Geller (1960)
Ga–O	MO_6	Ga_2O_3	Range: 1.95–2.08 Average: 2.00	Geller (1960)
In–O	MO_6	In_2O_3	Range: 2.13–2.23 Average: 2.18	Marezo (1966)
In–O	MO_7	$\text{WIn}_6\text{O}_{12}$	Range: 2.07–2.77 Average: 2.27	Michel and Kahn (1982)
In–O	MO_8	$\text{In}_2\text{Si}_2\text{O}_7$	Range: 2.04–2.36 Average: 2.28	Reid <i>et al.</i> (1977)
Sn–O	MO_6	SnO_2	Average: 2.05	Baur (1956)

2.09 Å are comparable those observed in β -gallia (2.00 Å) (10), SnO_2 (2.05 Å) (11) and In_2O_3 (2.18 Å) (12).

The MO_7 polyhedra show considerable distortion with respect to the fluorite parent structure with $M-O$ bond lengths of 2.023–2.561 Å. Similar distortions and In–O bond lengths were reported for WIn_6O_7 (13). The MO_7 polyhedra share edges with MO_8 polyhedra and MO_6 polyhedra and also share corners with MO_6 polyhedra.

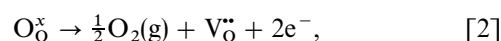
The InO_8 polyhedra are also distorted with respect to the MO_8 cubes in the parent structure. Oxygen atoms positioned across the face diagonals of the parent cube are either shifted towards one another or away from one another, resulting in half of In–O bonds having a length of 2.185 Å and the other half having a length of 2.570 Å. The coordination polyhedron is unlike that found in the $\text{Si}_2\text{In}_2\text{O}_7$ pyrochlore where the In–O bonds occur as six with a length of 2.356 Å and two with a length of 2.038 Å (14).

Implications of Structure on Conductivity

The tetragonal phase, $\text{Ga}_{3-x}\text{In}_{5+x}\text{Sn}_2\text{O}_{16}$, is a transparent conducting oxide (TCO) with conductivity on the order of 375 S/cm, approximately an order of magnitude lower than that of Sn-doped In_2O_3 . A primary factor accounting for the differences in conductivity is the ability of each phase to accept aliovalent dopants. In Sn-doped In_2O_3 , Sn^{4+} residing on In^{3+} acts as an electron donor, and the relatively high solubility of Sn in In_2O_3 (~6% on a cation basis) accounts for the relatively high conductivity of Sn-doped In_2O_3 . In $\text{Ga}_{3-x}\text{In}_{5+x}\text{Sn}_2\text{O}_{16}$, Sn is present primarily as a structural element. Attempts to dope $\text{Ga}_{3-x}\text{In}_{5+x}\text{Sn}_2\text{O}_{16}$ with excess Sn have shown that the solubility of Sn is much less than 1% on a cation basis, thereby limiting the achievable electrical conductivity (6).

We speculate that the ability of In_2O_3 to accept a relatively large amount of substituent Sn may be related to the anion arrangement around the sixfold-coordinated cations. As an illustration, consider the anion-deficient fluorite structures of In_2O_3 , $\text{Ga}_{3-x}\text{In}_{5+x}\text{Sn}_2\text{O}_{16}$, and $\text{In}_4\text{Sn}_3\text{O}_{12}$. Both $\text{Ga}_{3-x}\text{In}_{5+x}\text{Sn}_2\text{O}_{16}$ and $\text{In}_4\text{Sn}_3\text{O}_{12}$, which incorporate < 1% Sn as an aliovalent dopant (6, 15) have the MO_6 anion arrangement illustrated in Fig. 5a. In addition to the arrangement shown in Fig. 5a, In_2O_3 , which can incorporate up to 6% Sn, also has the MO_6 anion arrangement shown as Fig. 5b. If the latter site can accommodate higher levels of Sn, this may account for the higher conductivity of indium–tin–oxide (ITO). This needs to be confirmed by further studies.

On the other hand, the relatively good transparent conductivity of the T-phase apparently occurs without the benefit of Sn as a donor dopant. This is possible due to the ready formation of oxygen vacancies via



which occurs during the standard postprocessing reduction anneal typically employed for TCO materials. Alternative strategies for aliovalent doping in combination with the reduction reaction of Eq. [2] should be able to enhance the conductivity of the T-phase.

CONCLUSIONS

Using a combination of techniques, including high resolution electron microscopy, convergent beam electron diffraction, and Rietveld analysis of powder diffraction data (X-ray and time-of-flight neutron methods), the crystal structure of the transparent conductor, $\text{Ga}_{3-x}\text{In}_{5+x}\text{Sn}_2\text{O}_{16}$ ($x = 1.0$), was established. The tetragonal structure of this "T-phase" is derived from a cubic-fluorite parent structure by a 26.6° rotation about the c axis and removal of $\frac{1}{3}$ of the anions and belongs to the space group, $I4_1/a$. Refinements indicated size-dependent cation ordering, with complete occupation of the 4-fold $M(1)$ and 8-fold $M(2)$ positions by Ga and In, respectively, consistent with their ionic radii as compared to Sn. There is significant cation disorder on the 7-fold $M(3)$ sites (In predominantly, with some Sn) and the 6-fold $M(4)$ sites (all three cations), again consistent with ionic radii considerations. The M -O bond lengths were compared with known fluorite derivatives. The GaO_4 tetrahedra are essentially undistorted, with bond lengths comparable to those in $\beta\text{-Ga}_2\text{O}_3$. The MO_6 ($M = \text{Ga}, \text{In}, \text{Sn}$) polyhedra form distorted octahedra comparable to those observed in the parent oxides, $\beta\text{-Ga}_2\text{O}_3$, SnO_2 , and In_2O_3 . The distorted MO_7 ($M = \text{In}, \text{Sn}$) polyhedra are not found in the parent oxides, but are similar to those reported for WIn_6O_7 . The InO_8 polyhedra are distorted with respect to the MO_8 cubes in the parent structure, resulting in an equal split of In-O bond lengths of 2.185 and 2.570 Å. This behavior is related to, but distinct from, the behavior in the $\text{Si}_2\text{In}_2\text{O}_7$ pyrochlore, where a 6:2 division of bond lengths is observed.

The T-phase structure has potentially important ramifications for transparent conductivity. Of particular interest are the In positions and whether or not these can be substituted (doped) with Sn. The T-phase has the 7-fold $M(3)$ site in addition to one of the 6-fold sites (oxygen vacancies at

body-diagonal positions) observed in indium-tin-oxide. Apparently, neither of these positions is amenable to doping with an excess of Sn, i.e., the Sn solubility above the stoichiometric 20 cation percent is negligible. We speculate that the absence of the other 6-fold site in indium-tin-oxide (oxygen vacancies at face-diagonal positions) may be responsible for the inability to Sn-dope the T-phase.

ACKNOWLEDGMENTS

This work was supported by and largely conducted in facilities of the Materials Research Center at Northwestern University with support of the National Science Foundation under MRSEC Grant No. DMR-9632472. The support of the National Science Foundation through the Science and Technology Center for Superconductivity (DMR 91-20000) is also gratefully acknowledged (W.S. and L.D.M.). Some of the work was carried out at the Intense Pulsed Neutron Source at Argonne National Laboratory which is funded by the U.S. Department of Energy under Contract W-31-109-ENG-38. The authors thank Dr. Simine Short and Jim Jorgensen for their help with the neutron diffraction data.

REFERENCES

1. D. D. Edwards, T. O. Mason, F. Goutenoire, and K. R. Poeppelmeier, *Appl. Phys. Lett.* **70**(13), 1706 (1997).
2. J. D. Jorgensen, *J. Appl. Crystallogr.* **22**, 321 (1989).
3. A. C. Larson and R. B. Von Dreele, General Structure Analysis System, GSAS. Los Alamos National Laboratory, Los Alamos, NM.
4. A. C. Wilson, "International Tables for Crystallography," Vol. C. Kluwer Academic Publishers, Boston, 1995.
5. E. Hovestreydt, *Acta Crystallogr., Sect. A* **39**, 268 (1983).
6. D. D. Edwards and T. O. Mason, *J. Am. Ceram. Soc.* (1997). [Submitted]
7. B. F. Buxton, J. A. Eades, J. W. Steeds, and G. M. Rackham, *Phil. Trans. R. Soc. London* **281**, 171 (1976).
8. D. B. Williams and C. B. Carter, "Transmission Electron Microscopy," Vol. II. Plenum Press, New York, 1996.
9. J. Gjønnes and A. F. Moodie, *Acta Crystallogr.* **19**, 65 (1965).
10. S. Geller, *J. Chem. Phys.* **33**(3), 676 (1960).
11. V. W. H. Baur, *Acta Crystallogr.* **9**, 515 (1956).
12. M. Marezio, *Acta Crystallogr.* **20**, 723 (1966).
13. D. Michel and A. Kahn, *Acta Crystallogr., Sect. B.* **38**, 1437 (1982).
14. A. F. Reid, C. Li, and A. E. Ringwood, *J. Solid State Chem.* **20**, 219 (1977).
15. J. L. Bates, C. W. Griffin, D. D. Marchant, and J. E. Garneir, *Am. Ceram. Soc. Bull.* **65**(4), 673 (1986).